

# RSC Advances



This is an *Accepted Manuscript*, which has been through the Royal Society of Chemistry peer review process and has been accepted for publication.

*Accepted Manuscripts* are published online shortly after acceptance, before technical editing, formatting and proof reading. Using this free service, authors can make their results available to the community, in citable form, before we publish the edited article. This *Accepted Manuscript* will be replaced by the edited, formatted and paginated article as soon as this is available.

You can find more information about *Accepted Manuscripts* in the [Information for Authors](#).

Please note that technical editing may introduce minor changes to the text and/or graphics, which may alter content. The journal's standard [Terms & Conditions](#) and the [Ethical guidelines](#) still apply. In no event shall the Royal Society of Chemistry be held responsible for any errors or omissions in this *Accepted Manuscript* or any consequences arising from the use of any information it contains.

## Rheology, Thermal Property, and Foaming Behavior of High D-Content Poly(lactic Acid)/Cellulose Nanofiber Composites

WeiDan Ding<sup>a</sup>, Takashi Kuboki<sup>b</sup>, Anson Wong<sup>a</sup>, Chul B. Park<sup>a\*</sup>, Mohini Sain,<sup>c,d</sup>

<sup>a</sup> Microcellular Plastics Manufacturing Laboratory, Department of Mechanical and Industrial Engineering, University of Toronto, Toronto, Ontario, Canada M5S 3G8

<sup>b</sup> Department of Mechanical and Materials Engineering, Western University, London, Ontario, Canada, N6A 5B9

<sup>c</sup> Centre for Biocomposites and Biomaterials Processing, Faculty of Forestry, University of Toronto, Toronto, Ontario, Canada M5S 3B3

<sup>d</sup> KAU University, Jeddah, Saudi Arabia

\* Corresponding author (Chul B. Park, Email: park@mie.utoronto.ca, Tel: +1 416-978-3053)

### Abstract

Amorphous poly(lactic acid) (PLA)/cellulose nanofiber (CNF) composites were prepared using the solution casting method. We investigated the effects of the CNFs, which have aspect ratios over 100, on the PLA's rheological and thermal properties and on its foaming behavior. The rheological measurements showed that the incorporated CNFs substantially increased the PLA's viscosity in a low frequency range. This was attributed to both the interaction between the PLA molecular chains and the CNFs and the entanglement of CNFs. A batch foaming visualization system showed that the CNFs were effective cell-nucleating agents, and that they suppressed cell coalescence during the foaming process. In solid-state batch foaming processes, the addition of CNFs led to higher cell densities and decreased cell sizes in the composite foams. As the CNF content was increased, the cell-nucleating power and the resultant cell density increased. The cell sizes became more uniform. The improved foam morphology was also attributed to the CO<sub>2</sub>- and the CNF-induced crystallization during the gas-saturation and foaming processes. Thermal and wide angle X-ray diffraction (WAXD) analyses showed that the presence of CNFs and CO<sub>2</sub> enhanced the PLA's crystallization kinetics. An amorphous grade of PLA with a 12% D-content developed a high crystallinity of 21% after CO<sub>2</sub> gas saturation. The

formed crystals, especially those around the CNFs, promoted cell nucleation by local stress variations that were generated in the surrounding area. The crystals and CNFs also increased the PLA's viscosity, which restricted cell growth and reduced cell coalescence. On the other hand, due to increased stiffness, an excessive CNF content suppressed foaming.

**Keywords:** Cellulose nanofiber (CNF), Polylactic acid (PLA), Biocomposites, Rheology, Thermal property, Foaming

## 1. Introduction

Plastic is one of the most commonly used materials in the world, with applications ranging from household items to advanced engineering products. Most plastics used today are petrochemical-based. Meanwhile, in recent years, environmental consciousness,<sup>1,2</sup> technological improvement,<sup>3,4</sup> and stringent regulations<sup>5</sup> have significantly increased industrial interest in bio-based and biodegradable polymers. Polylactic acid (PLA), one of the most promising biodegradable polymers, is a bio-based plastic derived from renewable resources and consumes less nonrenewable energy during production compared with petrochemical-based polymers.<sup>6</sup> And it is readily biodegradable for waste disposal. It is widely used in the food packaging industry and in biomedical applications due to its biodegradability and biocompatibility.<sup>7-11</sup> However, neat PLA is brittle, and has low impact and tear resistance, a low heat deflection temperature, and a low crystallization rate.<sup>12-14</sup> To expand PLA's application areas, these deficiencies need to be mitigated.

The use of nano-scale fillers in plastics is a well-known method of addressing performance requirements, reducing costs, and/or improving processing ability. This strategy exploits such properties of nanoparticulates as a large surface area per mass, a high aspect ratio, and a low

percolation threshold.<sup>15</sup> Various nanoparticulates, including nanosilica, nanoclay, and carbon nanotubes (CNTs), have been added to PLA to enhance its mechanical strength,<sup>16-18</sup> thermal properties,<sup>17, 19, 20</sup> heat distortion temperature,<sup>16, 21</sup> gas barrier properties,<sup>16, 22</sup> electrical conductivity,<sup>18</sup> crystallization kinetics,<sup>23-28</sup> biodegradation rates,<sup>16, 19, 29</sup> flammability resistance,<sup>30</sup> and foaming behaviors.<sup>27, 28, 31-34</sup> Nevertheless, these nanoparticulates are inorganic materials and the potential health risk they pose from manufacturing to final disposal is considerable.<sup>35, 36</sup> On the contrary, cellulose nanofibers (CNFs), which are also described as nano-fibrillated cellulose,<sup>37-39</sup> are derived from renewable resources, and are nano-sized, lightweight, biocompatible, and biodegradable. There has been a growing interest in using CNFs as either additives or as reinforcement in various polymer systems to tailor polymers' performance.<sup>14, 40-46</sup> CNFs possess a Young's modulus of 115-150 GPa in the longitudinal direction and tensile strength of up to 2 GPa.<sup>44, 47-49</sup> These mechanical properties are comparable to, or even higher than those of high-strength glass fibers. The aspect ratio of CNFs was reported to be over 100.<sup>50</sup> It also has a very low coefficient of thermal expansion at  $10^{-7} \text{ K}^{-1}$  along the longitudinal direction.<sup>51</sup> Additionally, CNFs have significantly less cytotoxicity and genotoxicity compared with inorganic nanoparticulates.<sup>35, 52</sup> These intriguing properties make them an attractive component for high performance polymer nanocomposites. The incorporation of CNFs in PLA not only endows the resulting composites with fully biodegradable properties, but also gives them significantly improved mechanical properties.<sup>12, 14, 43, 45, 53</sup> Specifically, it has been demonstrated that the tensile modulus and the tensile strength of microfibrillated fibers reinforced PLA are doubled and tripled, respectively, when the fiber concentration is increased from 10 to 70 wt%.<sup>43</sup> The storage modulus of the PLA composites at 120°C was also improved about 3.5 fold with a fiber content of 20 wt%.<sup>45</sup>

Although the mechanical properties of CNF reinforced PLA have been remarkably improved, applications that require a low-density porous structure are still limited. For instance, in tissue engineering, a 3-D porous structure is essential for body cells to grow in a spatial environment,<sup>35, 54</sup> and a solvent-free fabrication method is preferred to produce a 3D structure for new tissue formation.<sup>55</sup> The microcellular foaming technology with CO<sub>2</sub>/N<sub>2</sub> as a blowing agent does not involve any organic solvents and, therefore, there is a significant advantage in the fabrication of biodegradable porous PLA material for bio-related applications. Thus, our study concentrates on the foaming behaviors of the PLA/CNF composites with CO<sub>2</sub>. There are only a few studies on the foaming of nano-sized cellulose fiber reinforced PLA biocomposites,<sup>41, 42, 56, 57</sup> where the effect of fibers varied. In the studies by Boissard et al.<sup>56</sup> and Cho et al.,<sup>57</sup> only a slight improvement, or even a deteriorated cell structure, was observed due to fiber aggregation.<sup>56, 57</sup> Dlouhá et al.<sup>41</sup> examined PLA batch foaming with 3–9 wt% CNFs under CO<sub>2</sub> pressures of 12–20 MPa and attributed the improved foam structure to the nucleating effect of the fibers and the enhanced PLA melting strength. Despite these earlier research efforts, the mechanism by which CNFs promote cell nucleation was still not clear, and the understanding of the effect of CO<sub>2</sub> on the PLA's crystallization and the crystallization's impact on foaming were lacking. Crystals, which can be generated during the gas-saturation stage, can significantly affect cell nucleation and the resulting morphology, especially through local stress variation and gas supersaturation.<sup>58-</sup><sup>64</sup> Cell nucleation and cell growth are two different stages, although they interact closely during the whole foaming process. In particular, when nucleating agents are present and the cells are expanding, the tensile stress generated in the particulates' vicinity promotes cell nucleation.<sup>65-68</sup> At the same time, a decrease in the local gas concentration due to enhanced cell nucleation suppresses cell growth. Meanwhile, cell growth can be affected by the amount of nucleating

agents and their intrinsic properties, the polymer viscosity, and the blowing agent's diffusivity in the polymer.<sup>65, 69, 70</sup> Thus, to understand the complex mechanism of the foaming process, an in-situ observation of foaming process is needed in order to clarify the role of the CNFs in the initial foaming stage.

In this study, an amorphous grade of PLA with 12% D-content was selected as the polymer matrix to compound with the CNFs through solution casting. We measured the rheological and thermal properties of the neat PLA and PLA/CNF biocomposites. Wide angle X-ray diffraction (WAXD) measurement was also used to analyze the crystal structure. Foaming experiments with neat PLA and PLA/CNF biocomposites were conducted with a batch foaming system and the effects of CNFs on the foaming behaviors of the PLA were identified. Foaming of the PLA/CNF biocomposites was also visualized in situ at a high temperature via a batch visualization system to help elucidate and decouple the effect of the crystals and CNFs on cell nucleation and cell growth during the initial stage of foaming.

## **2. Experimental**

### **2.1 Materials**

To study the effect of the CNFs on the foaming behavior, an amorphous PLA (NatureWorks LLC, Grade Ingeo™ 4060D) was chosen so that the crystallization effect could be minimized. The PLA has a density of 1.24 g/cm<sup>3</sup> and 12 % of D-lactide content. The melt flow index of this PLA is 15 g/10 min (190 °C/2.16 kg). Carbon dioxide (CO<sub>2</sub>) (99% pure, Linde Gas LLC) was used as a foaming agent. All materials were used as received without any further modification. The CNFs were extracted from wheat straw and obtained in aqueous suspension from the Centre for Biocomposites and Biomaterials Processing, University of Toronto. The manufacturing

process of CNFs was detailed in a previous study.<sup>50</sup> The CNFs have diameter and aspect ratios in the range of 10-80 nm and 90-110, respectively.<sup>50</sup>

## 2.2 Preparation of PLA/CNF biocomposites

The solvent exchange method was used to remove water prior to the mixing process. Specifically, an aqueous suspension of CNFs was first diluted with acetone, which was followed by centrifugation to extract the water. Next, the CNFs were dispersed thoroughly in the acetone in a container by continuous stirring with a magnetic stirrer at ambient temperature. During the stirring process, a measured amount of PLA was added gradually to maintain the CNF concentration at 0.1, 0.5, and 1 wt%. After the PLA's complete dissolution, a homogenizer was used to treat the mixture to obtain a homogeneous suspension. The suspension was poured into Petri dishes and left to dry at the room temperature. The composite film from the casting method was cut into small pieces. Then these were compression-molded into thin films at 180 °C. After hot pressing, the melted samples were removed and quickly quenched to obtain fully amorphous samples. The neat PLA was processed as described above to achieve the same process history as the composite materials. The dimensions of the plastic samples used in the visualization and solid-state foaming experiments were 6 × 0.1 (diameter × thickness) and 10 × 10 × 1 mm (width × length × thickness), respectively. In this study, PLA biocomposites with 0.1 wt%, 0.5 wt%, 1 wt%, and 3 wt% CNF content were labeled as PLA/CNF0.1, PLA/CNF0.5, PLA/CNF1, and PLA/CNF3, respectively.

## 2.3 CNF morphological characterization

The morphology of the CNFs was characterized using a field emission scanning electron microscope (SEM) (Hitachi S-5200) operated in a scanning transmission electron microscope

(STEM) mode (20kV). To study the CNF morphology, a drop of dilute CNF suspension was deposited on a carbon coated grid and allowed to dry at ambient temperature. To characterize the dispersion of the CNFs in the PLA matrix, the cryo-fractured surface of the PLA/CNF composite was subjected to a solvent vapour etching process using acetone. The samples were exposed to acetone vapours for around 12 hours at the ambient temperature. This process etched the PLA matrix and brought up the CNF domains, which led to a better contrast between the PLA and CNF phase. The etched samples were coated with a thin layer of platinum using a sputter coater (SC7620, Quorum Technologies) prior to examination using a SEM (JSM6610LV, JEOL).

## 2.4 Rheological characterization

Complex and steady shear viscosities of the PLA materials were determined using a rotational rheometer (ARES, TA Instruments) with a 25-mm parallel disk and a 1.0-mm gap. First, dynamic strain sweep tests were conducted to identify the strain limits of the linear viscoelastic region. Following this, a strain of 0.8 % was selected for all samples based on those strain limits. The dynamic frequency sweep experiments were then carried out to obtain the complex shear viscosity ( $\eta^*$ , Pa-s), storage modulus ( $G'$ ), and loss modulus ( $G''$ ) over a frequency range of 0.1–400 rad/s at 200 °C. The steady shear viscosity was also measured as a function of the shear rate in a range of 0.1–10 s<sup>-1</sup> so as to examine the shear thinning behavior of the neat PLA and the PLA/CNF composites.

## 2.5 Solid-state batch foaming process

The experiments were carried out as follows: First, samples were placed in a pressure chamber and saturated with CO<sub>2</sub> at a pressure of 5.52 MPa at the ambient temperature (~23 °C) for 24 hours (Figure 1a). According to the PLA-CO<sub>2</sub> sorption data reported in an earlier study,<sup>55</sup>

24 hours was a sufficient time to achieve the saturation equilibrium. Then, the CO<sub>2</sub>-saturated samples were taken out of the chamber immediately following a rapid release of the pressure. They were then dipped in a hot silicon oil bath at 100 °C for 20 seconds before being quenched in cold water to stabilize their foam morphology (Figure 1b). The samples' foaming was triggered by the rapid pressure drop and temperature rise. During these processes, the PLA's CO<sub>2</sub> solubility dropped significantly, and hence the samples became supersaturated and foaming was initiated. The cells were nucleated during the pressure drop, and they grew during the temperature increase stage as the polymer softened. Then, they finally solidified during the quenching process. Experiments were conducted four times for each material composition to examine the repeatability of the results.

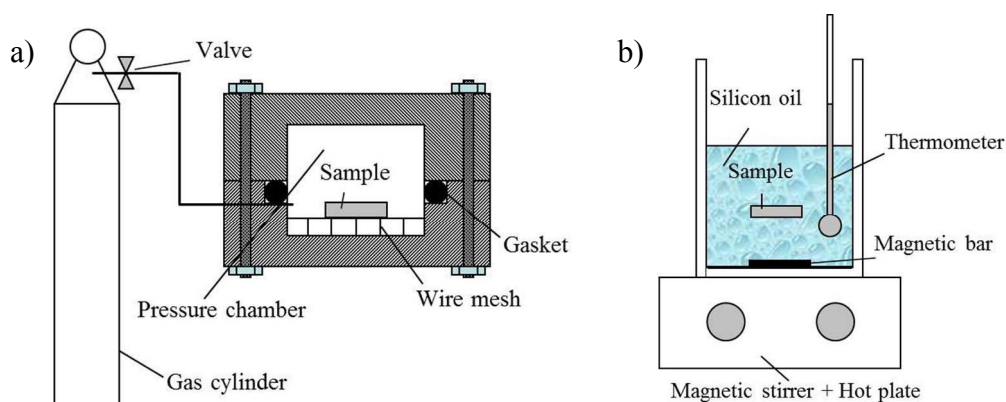


**Figure 1.** Schematic of a batch foaming process: a) Gas saturation process and b) Foaming process

## 2.6 In-situ foaming visualization

As Figure 2 shows, a batch foaming visualization system,<sup>71</sup> was used to observe the in-situ foaming behavior of the PLA/CNF/CO<sub>2</sub> system. The experiments were carried out as follows: First, a plastic sample was placed on top of a sapphire window inside a foaming chamber. Next, the chamber was sealed, and the temperature was increased to 200°C. After the system was

stabilized at 200°C, high pressure CO<sub>2</sub> was injected into the chamber at 5.52 MPa. The system was then maintained at 200 °C and 5.52 MPa for 30 minutes to allow the CO<sub>2</sub> to completely dissolve in the sample. Finally, the CO<sub>2</sub> was quickly released from the chamber via a release valve, and the samples were foamed during a rapid depressurization. At the same time, the foaming process was captured in situ by a high-speed camera, and the pressure-drop profile within the chamber was recorded. Experiments were conducted three times for each material composition to examine the repeatability of the results.

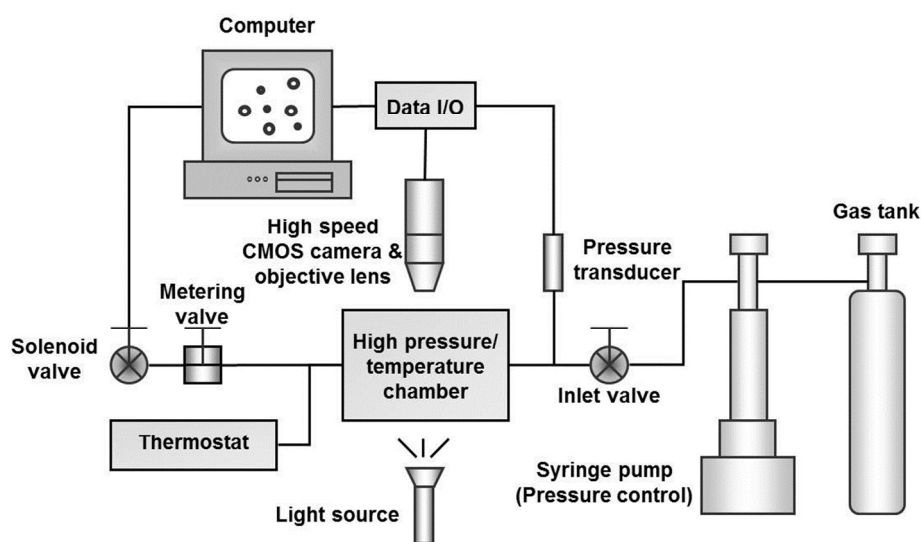


**Figure 2.** Schematic of a batch foaming visualization system<sup>71</sup>

## 2.7 Thermal analysis

The glass transition temperature ( $T_g$ ) of the neat PLA and PLA/CNF composites under atmospheric pressure (0.1 MPa) and at various CO<sub>2</sub> pressures (1.5, 3.0, 4.5, and 6.0 MPa) was investigated using a differential scanning calorimetry (DSC, TA Q2000) and a high-pressure DSC (NETZSCH DSC 204 HP Phoenix<sup>®</sup>, Germany), respectively. The  $T_g$ s were recorded during the cooling processes at a cooling rate of 5 °C/min.

The thermal properties and crystallization behaviors of the neat PLA, PLA/CNF composites, and their foamed counterparts were also evaluated using a DSC (TA Q2000). The samples after gas saturation were left at ambient temperature under atmospheric pressure for 1 week before any DSC analysis. This allowed the dissolved gas to completely diffuse out. The samples were scanned using a heating-cooling-heating cycle in a temperature range of 25–200°C. The heating and cooling rates were set at 10°C/min., and an isothermal treatment set at 200°C for 10 minutes was applied right after the first heating scan and prior to the second scan. This was to ensure that the samples had completely melted. The first heating scan was used to evaluate the samples' degree of crystallinity. The transition temperatures and enthalpies were determined from the thermograms. The PLA component's degree of crystallinity ( $X_c$ ) was calculated using Eq. (1) as follows:

$$X_c = (\Delta H / \Delta H^o) \times (1/w) \quad (1)$$

where  $\Delta H$  is the experimental heat of fusion determined from DSC,  $\Delta H^o$  is the heat of fusion of the fully crystalline PLA (93 J/g), and  $w$  is the weight fraction of the PLA in the biocomposites.

## 2.8 Wide angle X-ray diffraction (WAXD)

The X-ray diffraction patterns were collected on a Philips Analytical X-ray diffractometer (Almelo, Netherlands). A high resolution  $\text{CuK}\alpha$  source was used and operated at 40 KV and 40 mA. The scanned range for all samples was 5 – 35° ( $2\theta$ ) with a step size of 0.02 °/min and 2s per step. The obtained diffraction patterns were analyzed with X'Pert HighScore software. The specimens of the neat PLA and PLA/CNF05 composite with dimension of 10 × 10 × 1 mm were treated under various conditions for the WAXD test, and two specimens for each condition were used to examine the repeatability of the results.

## 2.9 Foam characterization

Foam density was measured using the water displacement method (ASTM D792-00). The expansion ratio ( $\Phi$ ) was then calculated according to Eq. (2) as follows:

$$\Phi = \rho_0 / \rho_f \quad (2)$$

where  $\rho_0$  is the bulk density of the PLA, or the PLA/CNF composites;  $\rho_f$  is the measured density of the foamed sample.

The foamed samples were cryo-fractured after immersion into liquid nitrogen to observe the cell morphology. The fractured surface was coated with a thin layer of platinum using a sputter coater (SC7620, Quorum Technologies), and the microstructure was examined using a scanning electron microscope (SEM) (JSM-6060, JEOL). For each sample, an area representing the typical cell morphology of the sample was chosen first, and then the cell sizes within that area were measured. Next, the cell size distribution of each material composition was determined. The cell densities with respect to the unfoamed volume ( $N_0$ ) were calculated from the SEM micrographs or camera snapshots using Eq. (3) as follows:

$$N_0 = (nM^2/A)^{3/2} \times \Phi \quad (3)$$

where  $n$  is the number of cells in the micrograph;  $A$  and  $M$  are the area and magnification factors of the micrograph, respectively; and  $\Phi$  represents the expansion ratio.

## 3. Results and Discussion

### 3.1 Morphology of CNFs and PLA/CNF biocomposites

Figure 3a shows the morphology of the received CNFs before mixing for composite preparation. The majority of CNFs had a diameter below 100 nm and their lengths measured

several micrometers. However, nanofiber bundles with a diameter of over 100 nm were also observed. Figures 3b and 3c show the cryo-fractured surfaces of the neat PLA and PLA/CNF3 composites after the solvent vapour etching process, respectively. Compared with the neat PLA, a number of white dots, which are the CNFs and CNF bundles, were observed on the surface of the PLA/CNF3 composites. From the image, it is clear that the CNFs were well dispersed in the PLA matrix. It is well-known that good CNF dispersion is critical to an efficient stress transfer from the matrix to the CNFs for mechanical performance improvement and to produce fine-celled foams.

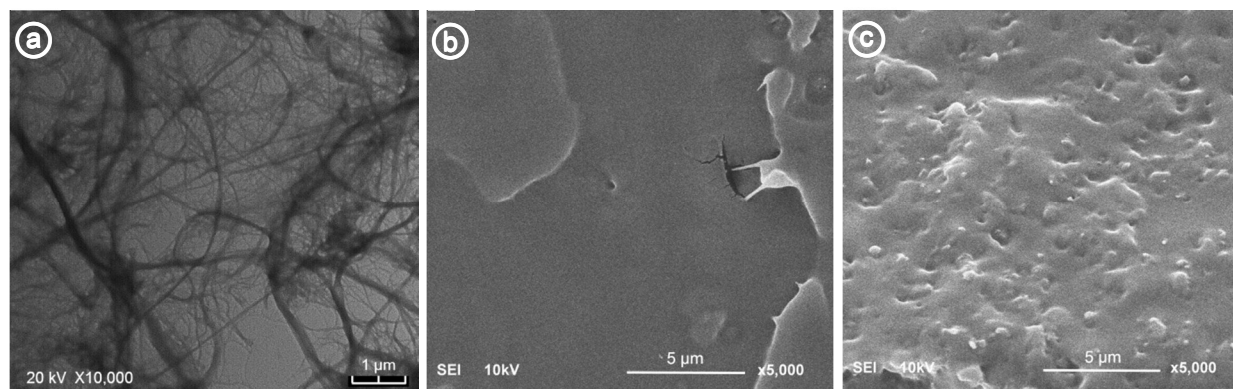


**Figure 3.** a) TEM images of the morphology of CNFs and SEM images of the cryo-fractured surface of b) neat PLA and c) PLA/CNF3 biocomposite

### 3.2 Rheological properties of the biocomposites

Figure 4 depicts the complex viscosity and the shear viscosity of the neat PLA and its biocomposites at 200°C. The complex viscosity increased with the CNF content, especially in a low frequency region (Figure 4a). As the frequency increased, the complex viscosity data converged to similar values. In a previous study, the high viscosity of the PLA/CNF composites was attributed to the interaction between the fibers through hydrogen bonding and good PLA/CNF interfacial bonding.<sup>57</sup> However, the hydrogen bonds were minimized in the current

study since the solvent-exchange method was used to produce the composites. Thus, the mechanical entanglement of the CNFs occurred due to their high aspect ratio and the good interaction between the PLA molecular chains and the CNFs were considered as the primary reasons for the increased complex viscosity. Neat PLA did not exhibit a clear shear thinning behavior in the studied shear rate range (Figure 4b). It was noted that the PLA/CNF0.1 composite's non-frequency dependence was similar to the neat PLA. However, at and above 0.5 wt% CNF content, the shear thinning behavior was much more pronounced, and the transition from the Newtonian plateau to the shear-thinning region shifted to a lower shear rate with an increased CNF content. In the case of 0.5, 1 and 3 wt% CNF contents, no evident Newtonian plateau was observed within the studied shear rate range. It has been reported that a network structure started to form at a CNF concentration of 0.5 wt%.<sup>72</sup> This shear-thinning behavior at low shear rates was largely due to the hindered mobility of the PLA molecular chain by a network-like structure of CNFs, so a higher shear stress and a more time were required for the composite to flow.<sup>73, 74</sup> On the other hand, at high shear rates, the CNFs tended to align preferentially along the shear direction, thereby decreasing the fiber-fiber interactions and hence the shear viscosity. Moreover, the neat PLA and its composites exhibited nearly the same viscosity at high shear rates. This result suggested that it is feasible to process high CNF content composites at a higher shear rate.

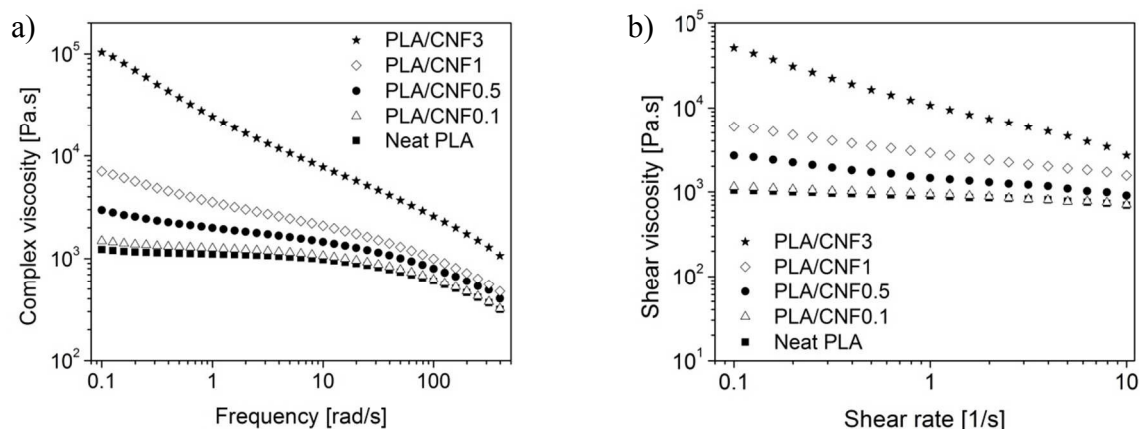


**Figure 4.** a) Complex viscosity and b) shear viscosity for neat PLA and PLA/CNF biocomposites

The storage ( $G'$ ) and loss ( $G''$ ) modulus against the frequency were plotted in Figure 5 to show the viscoelastic behaviors of neat PLA and its biocomposites. At high frequencies ( $>100$  rad/s), the viscoelastic behaviors of the neat PLA and PLA/CNF composites were similar, indicating that the impact of the CNFs was decreasing. At a low frequency ( $< 100$  rad/s), both moduli were less frequency-dependent with an increased CNF content, suggesting the CNF's influence. In the terminal region (low frequency), the slopes of both moduli were lower for PLA/CNF composites than for the neat PLA, especially for the composites with a CNF content over 0.5 wt%. The lessened frequency dependence of the PLA/CNF composites with an increased CNF content suggested a gradual change from the pseudoplastic-like to pseudosolid-like behavior. This reflected the formation of a 3D microstructure in the composites.<sup>16</sup> Due to the constraint generated by the spatially linked structure, the relaxation of these materials was largely prevented at a low frequency. Similar phenomena were observed in many other polymer nanocomposites previously.<sup>16, 75-77</sup> It can be seen that the crossover point of the  $G'$  and  $G''$  shifted to the left and upwards as the fiber content increased. The characteristic relaxation time can be estimated from the reciprocal of the lowest crossover frequency of the elastic and viscous

modulus by simply applying the power law fits to the data.<sup>78, 79</sup> Therefore, the relaxation times ( $\tau$ ) were calculated: 0.0028 s (neat PLA), 0.0031 s (0.1 wt%), 0.0036 s (0.5 wt%), 0.0050s (1 wt%), and 0.25s (3 wt%), respectively. The  $\tau$  increased with the fiber content, and this indicated an increased elasticity in the materials. The longer relaxation time favors the generation of higher local stress variations around the nucleating agents for cell nucleation during the foaming process.<sup>63</sup>

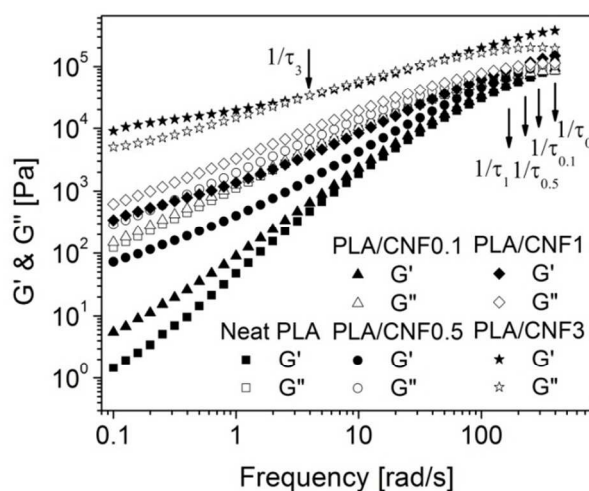


**Figure 5.** Storage ( $G'$ ) and loss modulus ( $G''$ ) as a function of frequency for neat PLA and PLA/CNF biocomposites (the arrows denote the lowest crossover frequencies corresponding with the reciprocal of the characteristic relaxation time)

The phase angle ( $\delta$ ) is the phase difference between the applied strain and measure stress, and  $\tan \delta$  is defined as the ratio of the loss modulus (viscous,  $G''$ ) to the storage modulus (elastic,  $G'$ ). The  $\delta$  or  $\tan \delta$  is also a measure to characterize the elastic response of the material (Figure 6). A completely elastic material will have a  $\delta = 0^\circ$ . As the material becomes more viscous, the  $\delta$  will tend towards  $90^\circ$ . As seen in Figure 6a, 0.5, 1, and 3 wt% of the CNF composite reached the highest  $\delta$  at frequencies of around 1.26, 3.16, and 12.59 rad/s. This is seen in comparison with the continuously rising  $\delta$  behavior for the neat PLA as the frequency decreased, which is

typically a pseudoplastic-like behavior in the terminal region.<sup>80</sup> In addition, the  $\tan \delta$  decreased considerably, and the plateau shape broadened with an increased CNF content. This decrease in  $\delta$  at low frequencies ( $< 10$  rad/s), suggested an increase in the terminal relaxation time. Similar behaviors were observed previously as the size of the macromolecule increased, that is, the increased molecular weight and level of the polymer chain branching.<sup>80, 81</sup> In this study, the decreased polymer chain mobility in the presence of the CNFs was the main reason for the increased relaxation time. At high CNF concentrations (of over 0.5 wt%), the value of  $\tan \delta$  became almost independent of the frequency (Figure 6a). This rheological behavior change was attributed to the formation of a 3D network structure caused by fiber-fiber interactions and/or fiber-polymer chain interactions.<sup>76</sup> The rheological CNF percolation concentration, which describes the above rheological property change, could be inferred from the loss tangent,  $\tan \delta = G''(\omega)/G'(\omega) = \text{constant}$ .<sup>77, 82-84</sup> We can identify this percolation concentration by plotting the  $\tan \delta$  as a function of the CNF content at a frequency range of 0.1–5 rad/s (Fig 6b). From the graph, the values of  $\tan \delta$  decayed gradually with an increased CNF content, and appeared to intersect at the CNF content ( $c_p$ ) of around 0.5 wt%. It was also observed that before reaching  $c_p$ , the value of  $\tan \delta$  decreased with an increased frequency, but after  $c_p$ , the trend reversed. These similar behaviors have been reported in several polymer nanocomposite systems.<sup>76, 77</sup>

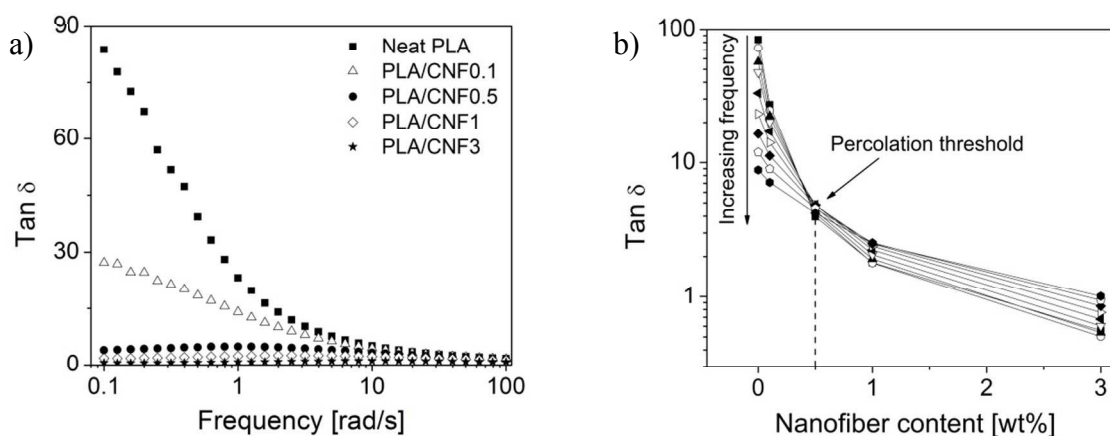


**Figure 6.** a)  $\tan \delta$  as a function of the frequency for neat PLA and PLA/CNF composites; and b)  $\tan \delta$  as a function of the nanofiber content; different lines represent different frequencies ranging from 0.1 to 5 rad/s

### 3.3 Thermal properties

The coupled effects of CNFs and dissolved CO<sub>2</sub> on  $T_g$  at various pressures were investigated, as Figure 7 shows. The  $T_g$  decreased linearly with an increased CO<sub>2</sub> pressure in all the PLA materials. The addition of CNFs did not have much effect on the  $T_g$  variations. Similar findings were found in our earlier study,<sup>25, 40, 85</sup> where semi-crystalline PLAs (4.5 % of D-lactide content) were used. The results suggested that the D-lactide content and the addition of various fillers (that is, CNFs, talc, nanosilica, or nanoclay) had little influence on the PLA's  $T_g$  variations. At the same saturation temperature, the amount of CO<sub>2</sub> dissolved in PLA increased linearly with pressure.<sup>86</sup> The  $T_g$  decreased due to the increased plasticization effect from the higher dissolved CO<sub>2</sub> content.<sup>87</sup> Therefore, a linear relationship was also expected for  $T_g$  suppression. It can be linearly extrapolated that the  $T_g$  was suppressed by around 15.2 °C, when the PLA samples were exposed to 5.52 MPa CO<sub>2</sub> pressure. Therefore, during the gas saturation process, the saturation temperature (that is, 23 °C) was around 7.8 °C higher than the  $T_g$  of the samples. This indicated that the incorporation of 5.52 MPa CO<sub>2</sub> had enhanced the PLA molecular chain mobility through its plasticizing effect, even at the ambient temperature. Thus, a decreased  $T_g$  was observed. The polymer chain's increased mobility could lead to a reduced energy requirement for PLA polymer chain folding and stacking (crystallization).<sup>25, 40, 85</sup>

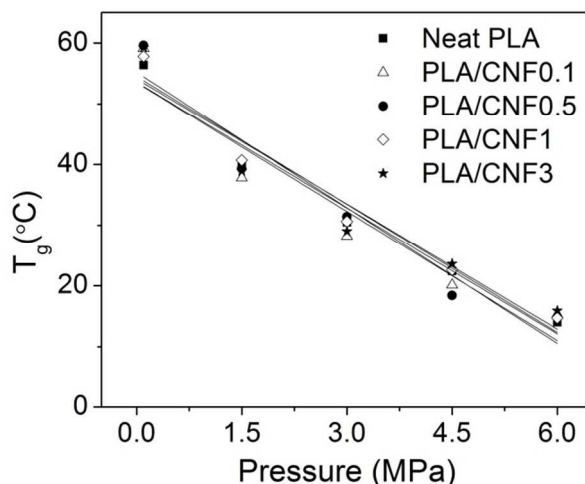


**Figure 7.** The  $T_g$  versus  $\text{CO}_2$  pressure for all Ingeo™ 4060D PLA samples at a cooling rate of  $5^\circ\text{C}/\text{min}$

We also studied the thermal properties and crystallization behaviors of neat PLA, PLA/CNF biocomposites, and the subsequent foams obtained from the heating-cooling-heating scan. A typical DSC thermogram for PLA/CNF1 was shown in Figure 8a, and similar curves were observed for other samples. The  $T_g$ , melting temperature ( $T_m$ ), and the  $X_c$  of the PLA materials before and after gas saturation and after foaming from the heating-cooling-heating scan were recorded and presented in Figure 8b, 8c, and 8d, respectively. The PLA's  $T_g$  and  $T_m$  can be observed in the thermograms for samples after gas saturation and foaming in the first heating run. However, only  $T_g$  could be observed for the PLA samples before saturation because the degree of crystallinity was negligible. Similarly, during the cooling and the second heating scans, no exothermic or endothermic peaks were observed except the peaks around  $T_g$  in all the samples.

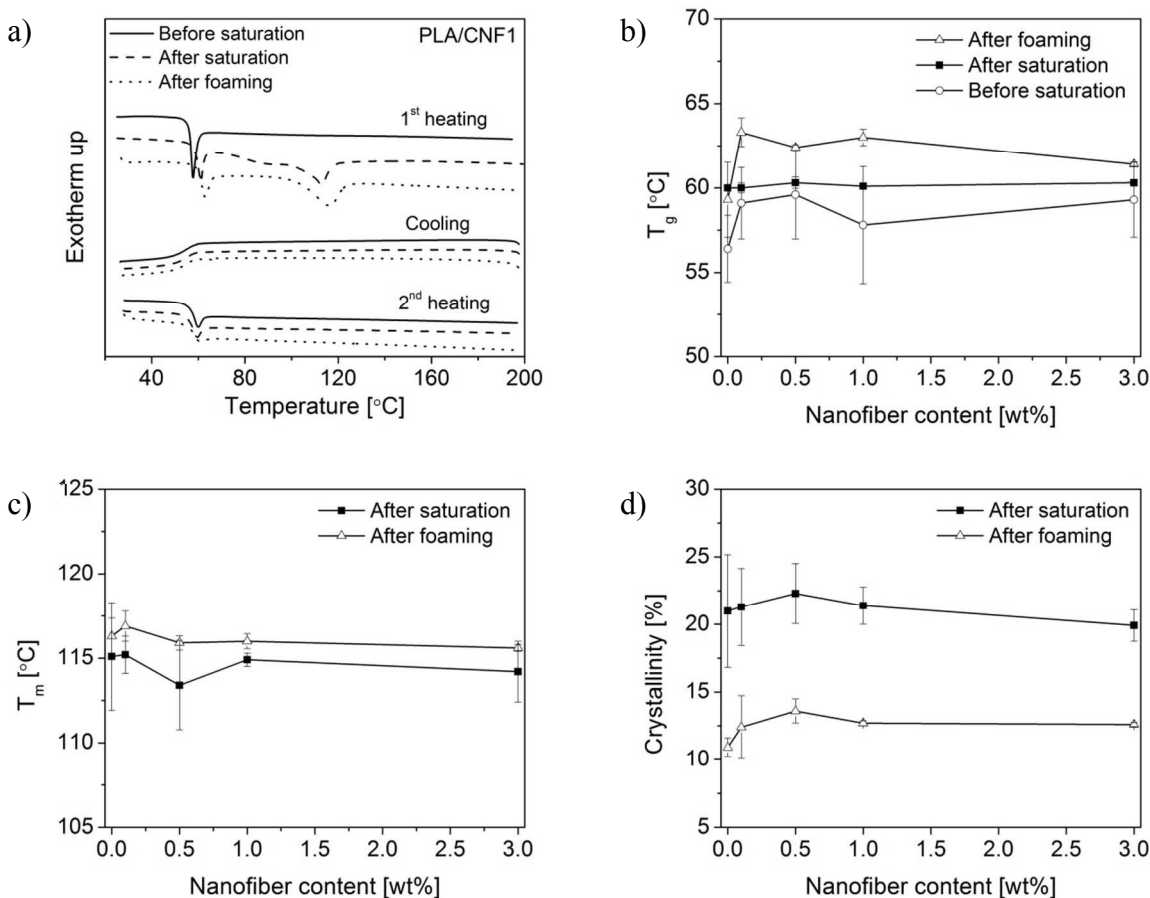


**Figure 8.** a) DSC 1<sup>st</sup> heating-cooling-2<sup>nd</sup> heating thermogram of PLA/CNF1 composites before gas saturation, and after gas saturation, and after foaming; b)  $T_g$  variation for the neat PLA and PLA/CNF nanocomposite; c)  $T_m$  and d) crystallinity of neat PLA and PLA/CNF nanocomposite, no melting peak and no crystallinity was detected for the samples before gas saturation

Although an amorphous grade of PLA was used in this study, the endothermic peaks corresponding to the melting of the majority of the PLA crystallites ( $T_m$ ) were observed around 115-120°C for the samples after both gas saturation and foaming. The degree of crystallinity was significantly higher for gas-saturated samples than for foamed samples (Figure 8d). The samples' crystallinity after gas saturation was around 21%, which was almost double of that of the corresponding foamed samples. It was notable that an unprecedentedly high crystallinity of 21% was achieved from the amorphous PLA of 12% D-lactide content, using CO<sub>2</sub> dissolution. As discussed earlier, dissolved CO<sub>2</sub> facilitated the PLA molecular chain mobility, and because such

polymer chains can fold and stack into a regularly packed structure, they increase crystallinity.<sup>40,</sup>  
<sup>85</sup> It has been reported that CNFs are effective crystal-nucleating agents and significantly change PLA's crystallization kinetics.<sup>40, 88</sup> However, the crystallinity did not change significantly in our study, as the CNF content was varied. It was speculated that the crystal size and distribution might be different between the neat PLA and the PLA/CNF composites, and this will be discussed further in the next section. Under the same processing conditions, a large number of densely-populated microcrystals were induced by CNFs in the PLA compared with the neat PLA.<sup>40</sup>

Figure 8a further illustrates that the saturated samples show another small peak around 85°C. Understandably, this small peak was due to the gas-induced imperfect crystals with a lower melting temperature. Compared with the saturated samples, only one melting peak was seen in the foamed sample. This could be largely attributed to the high oil bath temperature (100°C) used for the foaming experiment which partially melted the existing crystals at the low temperature. Further, the melting temperature of the foamed PLA samples was slightly higher than that of the saturated samples. This might have been due to the perfection of the loose-packed crystals, which were generated during the gas saturation process, pushing the  $T_m$  to a higher temperature. Overall, the foamed samples' crystallinity decreased due to the melted crystals which had a lower melting temperature. However, around 13 % of the crystallinity was still achieved for the foams due to the biaxial stretching of the polymer molecules during foam expansion and the biaxial stretching could have induced a higher degree of crystallization.<sup>61, 89, 90</sup>

Figure 8b shows that no significant  $T_g$  shift of PLA was observed for any samples. This could be attributed to the low weight fraction of the CNFs used in the composites. However, large variations of  $T_g$  for the samples before gas saturation were shown, even though there was no

significant difference among them. It is known that the  $T_g$  is affected by several factors, including molecular chain flexibility, molecular weight, intermolecular interaction, steric effects, and chain branching.<sup>91, 92</sup> The samples before gas saturation were obtained after the quick quenching of hot-pressed samples. We speculated that the PLA molecular chain mobility was affected by either the rapid temperature quenching or by the molecular chain interaction between the PLA and CNFs. Interestingly, compared with the samples before gas saturation, the saturated samples showed a slightly higher  $T_g$ . This might be attributed to the crystallization of samples during gas saturation. Moreover, the foamed composite samples had a higher  $T_g$  compared with their gas-saturated counterparts. This could be explained by the increased transcrystalline thickness around the CNFs due to the biaxial stretching and crystal perfection in the transcrystalline area during the foaming process, which would have further decreased the free volume in the polymer matrix. As a result, the chain mobility and flexibility were affected and more energy was required to break the confinement. In addition, the  $T_g$  of the foamed composite samples was higher than that of the foamed neat PLA, which probably resulted from the confinement of PLA molecules by dispersed CNFs. However, the  $T_g$  of the PLA/CNF3 composite foam was slightly lower than that of the other composite foams. It was speculated that a higher CNF content could have led to more agglomerations in the composites, which, in turn, could have reduced the interactions between the CNF and polymer molecular chains.

### 3.4 Wide angle X-ray diffraction (WAXD)

To acquire additional information on the crystallization behaviors of neat PLA and PLA/CNF composites, the crystalline structure of the PLA materials was characterized by wide angle X-ray diffraction (WAXD). Figure 9 shows the WAXD profiles of the neat PLA and the PLA/CNF composites before and after CO<sub>2</sub> gas saturation at the ambient temperature for 24 hours. A set of

compressed PLA specimens before gas saturation was also prepared as references and for comparison purposes (not shown). The unsaturated neat PLA and the PLA/CNF composites showed similar WAXD patterns without any crystalline peak, and thus, only one profile (labeled as “Amorphous”) was shown in Figure 9. Compared with the amorphous PLA materials, all gas-saturated specimens exhibited diffraction peaks at around  $2\theta = 15^\circ$ ,  $18.7^\circ$ ,  $22.4^\circ$ , and  $24^\circ$ . These diffraction peaks agreed well with the PLA  $\alpha$ -crystal, and were attributed to the reflections of (010), (203), (015), and (016) planes, respectively.<sup>40, 93-95</sup> Another reflection was located around  $2\theta = 16.3^\circ$  and was observed only in saturated PLA/CNF composites with a 0.5 wt% CNF content or greater. This indicated that the incorporation of CNFs increased the PLA’s crystallization ability. The diffraction peak, which was the result of the (110/200) plane reflection, had been identified as the  $\alpha''$ -crystal of PLA, which is a disordered  $\alpha$  form crystal.<sup>96, 97</sup> The molecular packing within the unit cell of an  $\alpha''$ -crystal was reported to be much looser and more disordered than in the  $\alpha$ - and the  $\alpha'$ -crystals.<sup>96, 97</sup> After gas release, the space that had been previously occupied by CO<sub>2</sub> during crystallization remained as voids in the crystalline region, and this led to the disordered  $\alpha''$ -crystal structure.<sup>97</sup> In addition, under the same condition, the crystal nucleation density was much higher in the PLA/CNF composites ( $\geq 0.5$  wt% CNF) than in the neat PLA and in the PLA/CNF01 composite due to the CNF’s significant crystal-nucleating effect.<sup>40</sup> The large amount of crystals might have generated a crystal network due to molecular entanglement.<sup>85</sup> This crystal network entanglement would greatly have increased the material’s viscosity and restricted the molecules to form new crystal layers. Therefore, a larger number of smaller crystals and looser crystal packing (that is, increased  $d$ -spacing) would occur in the PLA/CNF composites.

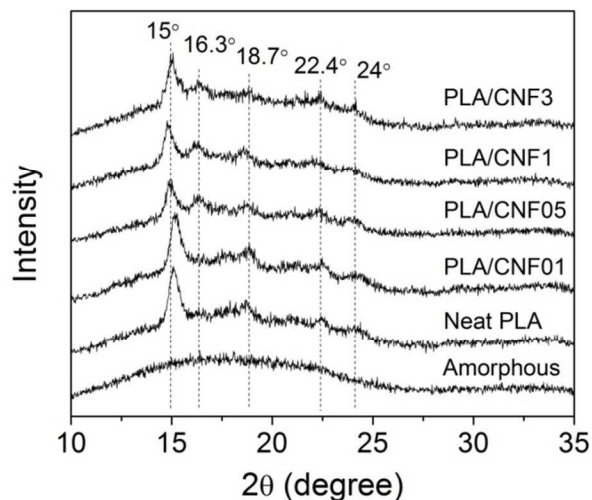


**Figure 9.** WAXD diffraction patterns of neat PLA and PLA/CNF composites before and after 5.52 MPa CO<sub>2</sub> gas saturation at ambient temperature for 24 hours, the PLA materials before gas saturation were labeled as “Amorphous”

### 3.5 In-situ foaming visualization

In order to study the effect of CNF content on the foaming behaviors of PLA, the saturation pressure ( $P$ ), the average pressure drop rate ( $-dP/dt|_{avg}$ ), and the system temperature ( $T_{sys}$ ) were kept constant at 5.52 MPa, 6.95 MPa/s, and 200°C, respectively. The levels of  $P$  and  $-dP/dt|_{avg}$  were selected at low levels, so that the gas-content and pressure-drop effects would not dominate the overall cell nucleation behaviors, and thereby weaken the effect of the fibers in the foaming processes.<sup>98, 99</sup> The CNF content was varied from 0 to 1 wt%. A high system temperature was chosen so that crystals would not exist during the foaming process. Consequently, the effect of fiber on the cell nucleation and growth phenomena could be investigated independently. Figure 10 shows the timeline from a series of videos for neat PLA and PLA/CNF composites at designated conditions, and only one set among 4 experimental runs. It shows the dynamic behavior of cell nucleation and growth in the early stage of the foaming processes. The cells

appeared as black dots due to light scattering and the bright regions were the polymer matrix. A comparison of the micrographs of samples with different fiber contents clearly showed that the number of nucleated cells in PLA increased as the CNF content increased (0–1 wt%). Figure 11 plots the cell density with respect to the unfoamed volume ( $N_{unfoamed}$ ) versus the time for different fiber content composites. The characterization was conducted based on the observable cells in the video. It is clear that the PLA/CNF composite had early onset cell nucleation and a higher cell density compared with the neat PLA, while the observable cell density increased as time elapsed for all three composites.

According to the classical<sup>62, 65, 100</sup> and modified<sup>67</sup> nucleation theory, if a cell, either preexisting or newly generated, becomes larger than a critical radius  $R_{cr}$ , it will grow spontaneously in order to minimize the free energy, whereas smaller cells will collapse. Assuming the polymer/gas mixture is a weak solution,  $R_{cr}$  can be expressed as a function of the interfacial tension at the liquid-gas interface ( $\gamma_{lg}$ ), the dissolved gas concentration ( $C$ ), and the local pressure ( $P_{local}$ ), which is given as follows:<sup>62, 63, 65, 67</sup>

$$R_{cr} = \frac{2\gamma_{lg}}{P_{cell} - P_{local}} = \frac{2\gamma_{lg}}{HC - P_{local}} = \frac{2\gamma_{lg}}{HC - (P_{sys} + \Delta P_{local})} \quad (4)$$

where  $H$  is the Henry's Law constant,  $P_{cell}$  is the hypothetical pressure inside the nucleated cell,  $P_{sys}$  is the average system pressure, and  $\Delta P_{local}$  is the local pressure (or negative stress) variations, that is, the difference between the local pressure  $P_{local}$  and  $P_{sys}$ . A cell is considered nucleated when  $R_{cr}$  becomes smaller than its current size, and thereby the cell is activated to grow.

A free energy barrier ( $W_{het}$ ) must be overcome for a cell to be nucleated heterogeneously and  $W_{het}$  can be estimated from the following equation:<sup>62, 63, 65, 67, 101</sup>

$$W_{het} = \frac{16\pi\gamma_{lg}^3 F(\theta_c, \beta)}{3(HC - (P_{sys} + \Delta P_{local}))^2} \quad (5)$$

$$F(\theta_c, \beta) = \frac{1}{4} \left[ 2 - 2\sin(\theta_c - \beta) + \frac{\cos\theta_c \cos^2(\theta_c - \beta)}{\sin\beta} \right] \quad (6)$$

where  $F(\theta_c, \beta)$  is a geometrical factor that relates to the surface geometry of the nucleating agents,  $\theta_c$  is the contact angle between the cell surface and the solid surface measured in the liquid phase, and  $\beta$  is the semi-conical angle of conical cavities that models the rough surface of the nucleating agents. Based on the heterogeneous cell nucleation theory, the presence of impurities in polymer would reduce the activation energy barrier for cell nucleation.<sup>65-67, 102</sup> The physical meaning of  $F(\theta_c, \beta)$  is the ratio of the volume of a heterogeneously nucleated cell (due to impurities) to the volume of a spherical cell with the same radius of curvature. The value of  $F(\theta_c, \beta)$  is typically smaller than 1. Therefore, a lower degree of supersaturation was required to nucleate new cells, which led to an earlier onset of cell nucleation and a higher cell nucleation rate.

From Eqs. (4) and (5), the  $R_{cr}$  and  $W_{het}$  change as  $\gamma_{lg}$  or  $C$  changes, and the cell nucleation rates change accordingly. For example, during the rapid system pressure drop in the foaming process, a sudden increase in the local  $\text{CO}_2$  concentration results in a higher degree of supersaturation, thus leading to more nucleated cells. The local pressure variation  $\Delta P_{local}$  can also significantly affect the cell nucleation rates.<sup>63, 65-67</sup> The growing cells generate local stress variations in the vicinity of the nucleating agents, which lead to a local pressure fluctuation. The  $\Delta P_{local}$  is positive if the local region experiences a compressive stress. It is negative if the local region is under an extensional stress. If there is extensional stress at the local region (that is,  $\Delta P_{local} < 0$ ),  $W_{het}$  and  $R_{cr}$  will decrease.<sup>65, 67</sup> Consequently, cell nucleation will be promoted. If the

magnitude of  $\Delta P_{local}$  is large due to the high viscosity or high elasticity, cell nucleation will be promoted.

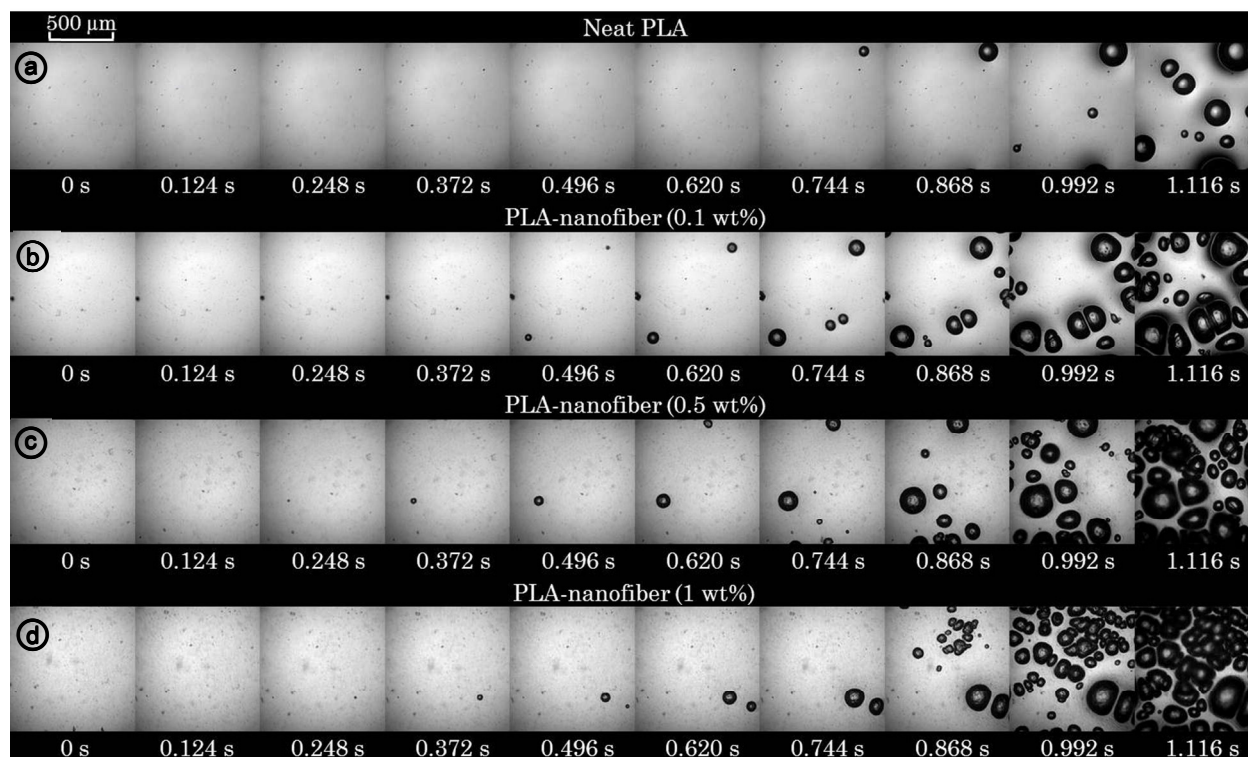


**Figure 10.** Snapshots of the PLA/CNF nanocomposite foaming video with various CNF contents, a) neat PLA, b) 0.1 wt%, c) 0.5wt%, and d) 1wt%

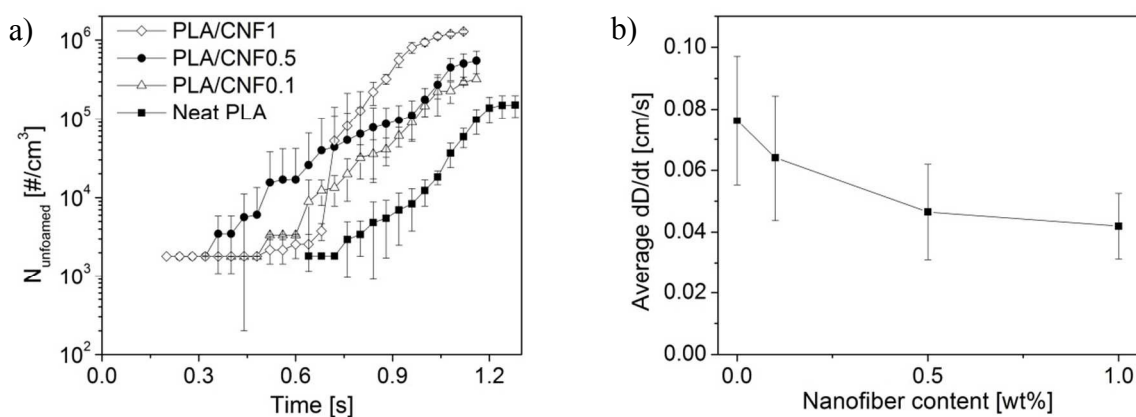


**Figure 11.** a) Cell density as a function of time and b) the average (-cell-diameter) growth rate for neat PLA and PLA/CNF biocomposites

From Figure 11a, the average maximum cell density with respect to the unfoamed volume ( $N_{unfoamed}$ ) for neat PLA was  $1.53 \times 10^4$  cells/cm<sup>3</sup>, and this increased to  $3.24 \times 10^5$ ,  $5.52 \times 10^5$ ,  $1.60 \times 10^6$  cells/cm<sup>3</sup>, respectively, when 0.1, 0.5, and 1 wt% of CNFs were added. The increased cell density with the CNFs was attributed to several factors. First, the large interfacial area between CNFs and the polymer provided more heterogeneous nucleating sites, which resulted in a high nucleation rate.<sup>69</sup> Second, there might have been pre-existing gas cavities at the polymer-fiber interface due to incomplete wetting. These gas cavities could potentially serve as seeds for cell nucleation. Specifically, a rapid pressure drop would induce a significant reduction in  $R_{cr}$ . When the  $R_{cr}$  dropped below the radii of the curvatures of the pre-existing gas cavities, these cavities would be activated and start to grow. Third, the pressure fluctuation around the CNFs would become more significant in the presence of nearby expanding cells that had been previously nucleated.<sup>66</sup> Thus, extensional stresses favorable for cell nucleation could be generated in that local region, as discussed above. Finally, an increase in the fiber content in the polymer matrix would have increased the complexity of the fiber network structure, and subsequently, it would have increased the polymer melt viscosity (Figure 4) which restricted cell growth (Figure 11b) and prevented cell coalescence and coarsening during the foaming processes. Due to a combination of the mechanisms discussed above, a higher cell density and a smaller cell size were observed for the PLA/CNF composite foams when compared with the neat PLA.

It is noteworthy that the cell density for 1 wt% PLA/CNF composite was lower than that of 0.1 or 0.5 wt% composites in the beginning ( $< 0.744$ s) and then increased sharply to the highest among the group. One possible explanation for this is that the formed nuclei were too small to be observable in the initial image due to the camera's resolution limit ( $\sim 2 \mu\text{m}$ ).<sup>64</sup> This could also

have been due to the low local pressure drop rate. CNFs used in the current study had very high aspect ratios (90-110), and they were entangled in the polymer matrix. As shown earlier, the percolation of the CNFs in the polymer matrix was around 0.5 wt% (Figure 6b). The fibers' entanglement might have led to different pressure drop variations in different regions when the system was subject to a rapid pressure drop. These pressure drop variations depended on the degree of the entanglement, that is, the complexity of the fiber network, which increased with the fiber content. Thus, cells were nucleated earlier in the high pressure-drop-rate regions than the others due to the larger reduction in  $R_{cr}$ . Eventually, cells would be nucleated in the low-pressure-drop rate region. Consequently, the cell density was still higher for the high-fiber content composites.

The average cell growth rates were determined from the growth profiles of 20 randomly selected cells in the neat PLA and PLA/CNF composites: 0.0762 cm/s (neat PLA), 0.0640 cm/s (PLA/CNF0.1), 0.0465 cm/s (PLA/CNF0.5), and 0.0419 cm/s (PLA/CNF1), respectively (Figure 11b). Analysis of variance (ANOVA) was performed to test the statistical significance of the impact of the CNF content on the cell growth rates. A  $p$ -value of  $< 0.001$  was obtained, which showed that the effect was significant. Therefore, it is concluded that the cell growth rates decrease with an increased CNF content. This could be the result of two mechanisms: 1) the increased viscosity of the composite melt with CNFs, which constrained cell growth during the foaming processes, as discussed above; and 2) a higher nucleation density with CNFs, resulting in more nucleated cells competing for gas to grow, which subsequently led to lower cell-growth rates.<sup>103</sup>

It is well-known that isothermal crystallization<sup>40, 85, 104</sup> and particulate-induced crystallization<sup>25, 40</sup> can occur in PLA under high-pressure CO<sub>2</sub>. However, due to the high

operating temperature adopted in the foaming experiments, it is believed that all crystals were completely melted even if there were any crystals that were formed during the heating stage. Therefore, we concluded that the increased cell density and decreased cell size with an increasing CNF content was due to the effect of the CNFs.

### 3.6 Solid-state batch foaming

Figure 12 presents the foam morphology of PLA and its fiber composites (core part) after batch foaming with different CNF contents. Poor cell morphology was observed in the neat PLA sample (Figure 12a). The cell structures were improved and the cell size distribution became more uniform as the fiber content increased (Figure 12b–f). Figure 13 shows the effects of the CNF content on cell size distribution, the cell densities (with respect to the unfoamed volume), and the average volume expansion ratios. The cell density increased remarkably from  $7.5 \times 10^6$  cells/cm<sup>3</sup> for the neat PLA to  $3.7 \times 10^7$ ,  $5.6 \times 10^7$ ,  $4.3 \times 10^8$ , and  $2.5 \times 10^{11}$  cells/cm<sup>3</sup>, respectively, when the CNFs of 0.1, 0.5, 1, and 3 wt% were added, as observed by others.<sup>41, 42, 46</sup> The average expansion ratios were maintained at around 8 for neat PLA and composites with a CNF content up to 0.5 wt%. However, at 1 and 3 wt% of the CNFs, this ratio decreased significantly to 2.6 and 1.1, respectively. Because of the percolation of the fibers in the polymer matrix (see Figure 6b), a large expansion ratio could not be achieved, a scattering of isolated cells was observed, and some sections did not foam at all.

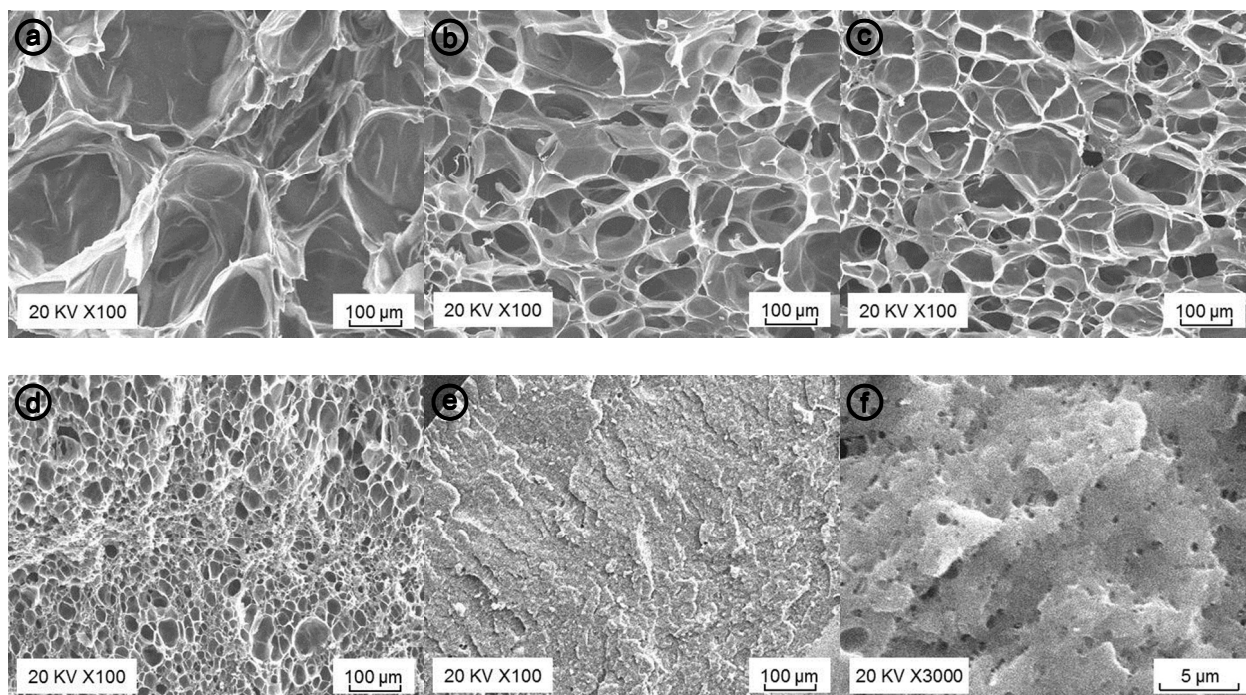


**Figure 12.** SEM images of the PLA/CNF nanocomposite foams with different CNF contents: a) 0 wt%; b) 0.1 wt%; c) 0.5 wt%; d) 1 wt%; e & f) 3 wt% with different magnifications

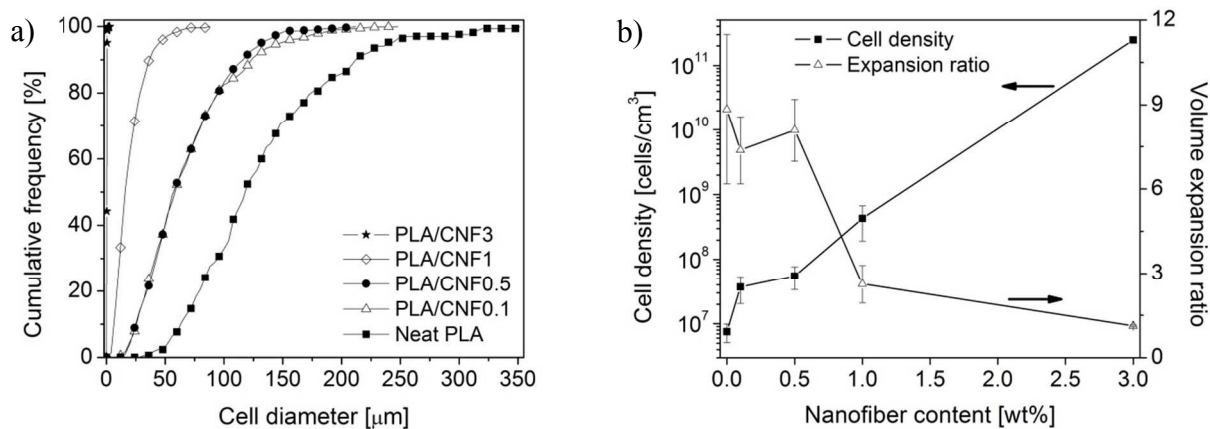


**Figure 13.** a) Cell size distribution and b) volume expansion ratio and cell density of neat PLA and PLA/CNF nanocomposite foams

It is believed that, besides the CNFs, the crystals generated in PLA have also affected the cell morphology in the solid-state batch foaming process conducted at 100°C. This is unlike the case of in-situ visualization experiments conducted at 200°C, where all crystals were melted. The DSC thermal analysis (Figure 8d) showed there was indeed a sizable amount of crystals in the

gas-saturated neat PLA and its composites. Therefore, the results shown in Figure 13b do not simply indicate that CNF is the only factor affecting the cell density and expansion ratio. The crystals induced by CNFs and CO<sub>2</sub> gas must also have affected the PLA's foaming behaviors.<sup>40,</sup>

88

The crystallization of PLA affects its cell nucleation and cell growth behaviors significantly. According to Eqs. (4) and (5), crystals can affect cell nucleation, especially through the local stress variations and gas supersaturation.<sup>59, 60, 63, 65</sup> The formed or growing crystals can generate local stresses because polymer chains in the amorphous region are constrained by the adjacent crystals due to the crystal contraction.<sup>63</sup> The growing cells can cause the deformation of the surrounding polymer chains, while crystals are restricted from movement due to their rigidity and connections to other polymer chains.<sup>63, 65</sup> Consequently, tensile stresses would also be generated around the formed crystals. Cell nucleation can be promoted in these tensile stress fields. The growing crystals can expel the dissolved CO<sub>2</sub> into the crystalline-amorphous phase interface; hence, the interface region becomes supersaturated with CO<sub>2</sub> and the preferential cell nucleation sites.<sup>59, 63</sup> The induced crystals can increase the PLA's melt strength through the connection of the molecules via crystals. The enhancement of melt strength can decrease the cell growth rate and prevent the cell wall opening.<sup>105</sup>

In the current study, the crystals could be induced in several ways. First, CO<sub>2</sub> gas saturation promoted the PLA's crystallization, as discussed in the Section of thermal properties. Second, CNFs induced a large number of densely-populated microcrystals in the PLA, as reported in our earlier study.<sup>40</sup> Finally, during the foaming process in the oil bath, cold crystallization might have occurred, and new crystals could be generated due to the increased polymer chain mobility. As discussed earlier, these CO<sub>2</sub>- and CNF- induced crystallization in PLA during gas saturation

and cold crystallization during foaming could enhance cell nucleation significantly. Therefore, more gas was used for cell nucleation and subsequently less gas was available for cell growth.<sup>106</sup> On the other hand, the increase in PLA's viscosity due to CNFs and induced crystals restricted cell growth and prevented coalescence and coarsening. These combined factors produced a high cell density with a smaller cell size in the final foams, especially with CNFs.

The average volume expansion ratio was also affected and showed a notable drop when 1 wt% of or more CNFs was added. We noted that too high a CNF content (that is, 3 wt%) resulted in non-uniform foam structures in the composite. This could be attributed to the non-uniform fiber dispersion in PLA and to the extreme high viscosity of the composite. High viscosity could suppress foaming in the CNF-rich regions (that is, over 3 wt%) and restrict cell growth in the CNF-less area (< 3 wt%). This indicated that a high CNF content increased the difficulty of dispersing CNF into the polymer matrix. Nevertheless, the small cells generated from the PLA/CNF3 suggested that it is possible to generate high-density PLA foams with a submicron or a nano-cell structure.

#### 4. Conclusions

The effects of CNFs on the rheological and thermal properties and foaming behaviors of PLA have been investigated. The SEM study showed that the CNFs were well dispersed in the PLA matrix. The PLA's viscosity increased considerably with an increased CNF content. A gradual change from a pseudoplastic-like to a pseudosolid-like relaxation behavior with an increased CNF content was observed. This was due to the formation of 3D structure network of CNFs and a good interaction between the PLA molecular chains and the CNFs. In the in-situ foaming visualization experiment, CNFs served as effective nucleating agents for enhanced cell

nucleation during the foaming process. The cell growth rate, cell coalescence, and cell coarsening were suppressed greatly due to the significant increase in the PLA's melt strength by the addition of CNFs. In solid-state batch foaming, the incorporation of CNFs led to a higher cell density and a smaller cell size compared with neat PLA foam. This was attributed to the cell nucleating effects of the CNFs and the formed crystals, as well as the suppressed cell deterioration through the increased melt strength of PLA with added CNFs and crystals. DSC analysis showed that a high crystallinity of 21% had been achieved after a CO<sub>2</sub> gas saturation for an amorphous grade of PLA with a 12% D-content. WAXD measurement indicated that a disordered crystal structure was generated during the gas saturation process. However, 3 wt% CNF suppressed the foaming and resulted in isolated and scattered cells in the composite due to a non-uniform fiber dispersion and an extremely high melt viscosity.

### Acknowledgements

The authors are grateful for the financial support provided by the National Sciences and Engineering Research Council of Canada (NSERC), the Ontario Graduate Scholarship Program, the AUTO21, the Consortium for Cellular and Micro-Cellular Plastics (CCMCP), and the Centre for Biocomposites and Biomaterials Processing (CBBP), University of Toronto.

### References

1. M. Poliakov, J. M. Fitzpatrick, T. R. Farren and P. T. Anastas, *Science*, 2002, **297**, 807-810.
2. T. Gerngross, S. Slater, R. A. Gross and B. Kalra, *Science*, 2003, **299**, 822-825.
3. R. E. Drumright, P. R. Gruber and D. E. Henton, *Adv. Mater.*, 2000, **12**, 1841-1846.
4. E. T. H. Vink, K. R. Rábago, D. A. Glassner, B. Springs, R. P. O'Connor, J. Kolstad and P. R. Gruber, *Macromol. Biosci.*, 2004, **4**, 551-564.
5. S. I. Sakai, H. Yoshida, J. Hiratsuka, C. Vandecasteele, R. Kohlmeyer, V. S. Rotter, F. Passarini, A. Santini, M. Peeler, J. Li, G. J. Oh, N. K. Chi, L. Bastian, S. Moore, N. Kajiwara, H. Takigami, T. Itai, S. Takahashi, S. Tanabe, K. Tomoda, T. Hirakawa, Y. Hirai, M. Asari and J. Yano, *J. Mater. Cycles Waste Manage.*, 2014, **16**, 1-20.

6. E. T. H. Vink, S. Davies and J. J. Kolstad, *Industrial Biotechnology*, 2010, **6**, 212-224.
7. K. Parker, J. P. Garancher, S. Shah and A. Fernyhough, *J. Cell. Plast.*, 2011, **47**, 233-243.
8. J. W. Rhim and J. H. Kim, *J. Food Sci.*, 2009, **74**, E105-E111.
9. J. H. Schut, *Plastics Technology*, 2007, **53**, 39-43.
10. C. A. García-González, A. Vega-González, A. M. López-Periago, P. Subra-Paternault and C. Domingo, *Acta Biomater.*, 2009, **5**, 1094-1103.
11. K. Zhang, H. Wang, C. Huang, Y. Su, X. Mo and Y. Ikada, *Journal of Biomedical Materials Research - Part A*, 2010, **93**, 984-993.
12. L. Suryanegara, H. Okumura, A. N. Nakagaito and H. Yano, *Cellulose*, 2011, **18**, 689-698.
13. K. Zhang, A. K. Mohanty and M. Misra, *ACS Appl. Mater. Interfaces*, 2012, **4**, 3091-3101.
14. L. Suryanegara, A. N. Nakagaito and H. Yano, *Cellulose*, 2010, **17**, 771-778.
15. E. Manias, *Nat. Mater.*, 2007, **6**, 9-11.
16. S. Sinha Ray and M. Okamoto, *Macromol. Rapid Commun.*, 2003, **24**, 815-840.
17. B. K. Chen, C. C. Shih and A. F. Chen, *Compos. Part A: Appl. S.*, 2012, **43**, 2289-2295.
18. R. Rizvi, J. K. Kim and H. Naguib, *Smart Mater. Struct.*, 2010, **19**.
19. M. Panigrahi, N. K. Singh, R. K. Gautam, R. M. Banik and P. Maiti, *Compos. Interfaces*, 2010, **17**, 143-158.
20. J. Zhang, J. Lou, S. Ilias, P. Krishnamachari and J. Yan, *Polymer*, 2008, **49**, 2381-2386.
21. C. F. Kuan, C. H. Chen, H. C. Kuan, K. C. Lin, C. L. Chiang and H. C. Peng, *J. Phys. Chem. Solids*, 2008, **69**, 1399-1402.
22. P. Maiti, K. Yamada, M. Okamoto, K. Ueda and K. Okamoto, *Chem. Mater.*, 2002, **14**, 4654-4661.
23. S. Barrau, C. Vanmansart, M. Moreau, A. Addad, G. Stoclet, J. M. Lefebvre and R. Seguela, *Macromolecules*, 2011, **44**, 6496-6502.
24. J. Y. Nam, S. Sinha Ray and M. Okamoto, *Macromolecules*, 2003, **36**, 7126-7131.
25. M. Nofar, A. Tabatabaei and C. B. Park, *Polymer*, 2013, **54**, 2382-2391.
26. S. Saeidlou, M. A. Huneault, H. Li and C. B. Park, *Prog. Polym. Sci.*, 2012, **37**, 1657-1677.
27. A. Ameli, D. Jahani, M. Nofar, P. U. Jung and C. B. Park, *Compos. Sci. Technol.*, 2014, **90**, 88-95.
28. A. Ameli, M. Nofar, D. Jahani, G. Rizvi and C. B. Park, *Chem. Eng. J.*, 2015, **262**, 78-87.
29. S. Bocchini, K. Fukushima, A. Di Blasio, A. Fina, A. Frache and F. Geobaldo, *Biomacromolecules*, 2010, **11**, 2919-2926.
30. T. D. Hapuarachchi and T. Peijs, *Compos. Part A: Appl. S.*, 2010, **41**, 954-963.
31. Y. Fujimoto, S. Sinha Ray, M. Okamoto, A. Ogami, K. Yamada and K. Ueda, *Macromol. Rapid Commun.*, 2003, **24**, 457-461.
32. M. Nofar and C. B. Park, *Prog. Polym. Sci.*, 2014, **39**, 1721-1741.
33. M. Keshtkar, M. Nofar, C. B. Park and P. J. Carreau, *Polymer*, 2014, **55**, 4077-4090.
34. S. Pilla, S. G. Kim, G. K. Auer, S. Gong and C. B. Park, *Materials Science and Engineering: C*, 2010, **30**, 255-262.
35. M. J. D. Clift, E. J. Foster, D. Vanhecke, D. Studer, P. Wick, P. Gehr, B. Rothen-Rutishauser and C. Weder, *Biomacromolecules*, 2011, **12**, 3666-3673.
36. L. Reijnders, *J. Mater. Sci.*, 2012, **47**, 5061-5073.
37. K. Missoum, M. N. Belgacem and J. Bras, *Materials*, 2013, **6**, 1745-1766.
38. H. P. S. Abdul Khalil, Y. Davoudpour, M. N. Islam, A. Mustapha, K. Sudesh, R. Dungani and M. Jawaid, *Carbohydr. Polym.*, 2014, **99**, 649-665.
39. S. Kalia, S. Boufi, A. Celli and S. Kango, *Colloid. Polym. Sci.*, 2014, **292**, 5-31.

40. W. D. Ding, R. K. M. Chu, L. H. Mark, C. B. Park and M. Sain, *Eur. Polym. J.*, 2015, **71**, 231-247.
41. J. Dlouhá, L. Suryanegara and H. Yano, *Soft Matter*, 2012, **8**, 8704-8713.
42. J. Dlouhá, L. Suryanegara and H. Yano, *React. Funct. Polym.*, 2014, **85**, 201-207.
43. A. N. Nakagaito, A. Fujimura, T. Sakai, Y. Hama and H. Yano, *Compos. Sci. Technol.*, 2009, **69**, 1293-1297.
44. A. N. Nakagaito and H. Yano, *Appl. Phys. A: Mater. Sci. Process.*, 2005, **80**, 155-159.
45. L. Suryanegara, A. N. Nakagaito and H. Yano, *Compos. Sci. Technol.*, 2009, **69**, 1187-1192.
46. N. Zhao, L. H. Mark, C. Zhu, C. B. Park, Q. Li, R. Glenn and T. R. Thompson, *Ind. Eng. Chem. Res.*, 2014, **53**, 11962-11972.
47. Y. Nishiyama, *J. Wood Sci.*, 2009, **55**, 241-249.
48. B. Wang and M. Sain, *Compos. Sci. Technol.*, 2007, **67**, 2521-2527.
49. I. Diddens, B. Murphy, M. Krisch and M. Müller, *Macromolecules*, 2008, **41**, 9755-9759.
50. A. Alemdar and M. Sain, *Compos. Sci. Technol.*, 2008, **68**, 557-565.
51. T. Nishino, I. Matsuda and K. Hirao, *Macromolecules*, 2004, **37**, 7683-7687.
52. R. de Lima, L. O. Feitosa, C. R. Maruyama, M. A. Barga, P. C. Yamawaki, I. J. Vieira, E. M. Teixeira, A. C. Corrêa, L. H. Caparelli Mattoso and L. F. Fraceto, *Int. J. Nanomedicine*, 2012, **7**, 3555-3565.
53. A. Iwatake, M. Nogi and H. Yano, *Compos. Sci. Technol.*, 2008, **68**, 2103-2106.
54. J. J. Blaker, K. Y. Lee, A. Mantalaris and A. Bismarck, *Compos. Sci. Technol.*, 2010, **70**, 1879-1888.
55. X. Wang, W. Li and V. Kumar, *Biomaterials*, 2006, **27**, 1924-1929.
56. C. I. R. Boissard, P. E. Bourban, C. J. G. Plummer, R. C. Neagu and J. A. E. Månson, *J. Cell. Plast.*, 2012, **48**, 445-458.
57. S. Cho, H. Park, Y. Yun and H.-J. Jin, *Macromol. Res.*, 2013, **21**, 529-533.
58. Q. Ren, J. Wang, W. Zhai and S. Su, *Ind. Eng. Chem. Res.*, 2013, **52**, 13411-13421.
59. K. Taki, D. Kitano and M. Ohshima, *Ind. Eng. Chem. Res.*, 2011, **50**, 3247-3252.
60. G. Ji, W. Zhai, D. Lin, Q. Ren, W. Zheng and D. W. Jung, *Ind. Eng. Chem. Res.*, 2013, **52**, 6390-6398.
61. M. Mihai, M. A. Huneault and B. D. Favis, *J. Appl. Polym. Sci.*, 2009, **113**, 2920-2932.
62. S. N. Leung, A. Wong, Q. Guo, C. B. Park and J. H. Zong, *Chem. Eng. Sci.*, 2009, **64**, 4899-4907.
63. A. Wong, Y. Guo and C. B. Park, *J. Supercrit. Fluids*, 2013, **79**, 142-151.
64. A. Wong and C. B. Park, *Polym. Test.*, 2012, **31**, 417-424.
65. S. N. Leung, A. Wong, L. C. Wang and C. B. Park, *J. Supercrit. Fluids*, 2012, **63**, 187-198.
66. C. Wang, S. N. Leung, M. Bussmann, W. T. Zhai and C. B. Park, *Ind. Eng. Chem. Res.*, 2010, **49**, 12783-12792.
67. A. Wong, S. L. Wijnands, T. Kuboki and C. B. Park, *J. Nanopart. Res.*, 2013, **15**, 1815-1829.
68. A. Wong and C. B. Park, *Chem. Eng. Sci.*, 2012, **75**, 49-62.
69. K. Taki, T. Yanagimoto, E. Funami, M. Okamoto and M. Ohshima, *Polym. Eng. Sci.*, 2004, **44**, 1004-1011.
70. A. Wong, L. H. Mark, M. M. Hasan and C. B. Park, *The Journal of Supercritical Fluids*, 2014, **90**, 35-43.
71. Q. Guo, J. Wang, C. B. Park and M. Ohshima, *Ind. Eng. Chem. Res.*, 2006, **45**, 6153-6161.

72. P. Chen, H. Yu, Y. Liu, W. Chen, X. Wang and M. Ouyang, *Cellulose*, 2013, **20**, 149-157.
73. K. Lozano, J. Bonilla-Rios and E. V. Barrera, *J. Appl. Polym. Sci.*, 2001, **80**, 1162-1172.
74. A. Kiziltas, B. Nazari, D. J. Gardner and D. W. Bousfield, *Polym. Eng. Sci.*, 2014, **54**, 739-746.
75. G. Galgali, C. Ramesh and A. Lele, *Macromolecules*, 2001, **34**, 852-858.
76. V. Khoshkava and M. R. Kamal, *ACS Appl. Mater. Interfaces*, 2014, **6**, 8146-8157.
77. A. Rizvi and C. B. Park, *Polymer*, 2014, **55**, 4199-4205.
78. X. Zhu, B. Kundukad and J. R. C. Van Der Maarel, *J. Chem. Phys.*, 2008, **129**, doi: 10.1063/1061.3009249.
79. A. J. Hsieh, P. Moy, F. L. Beyer, P. Madison, E. Napadensky, J. Ren and R. Krishnamoorti, *Polym. Eng. Sci.*, 2004, **44**, 825-837.
80. S. Li, M. Xiao, D. Wei, H. Xiao, F. Hu and A. Zheng, *Polymer*, 2009, **50**, 6121-6128.
81. D. Graebing, *Macromolecules*, 2002, **35**, 4602-4610.
82. R. Muller, E. Gerard, P. Dugand, P. Rempp and Y. Gnanou, *Macromolecules*, 1991, **24**, 1321-1326.
83. H. H. Winter, *Polym. Eng. Sci.*, 1987, **27**, 1698-1702.
84. H. Winter and M. Mours, in *Neutron Spin Echo Spectroscopy Viscoelasticity Rheology*, Springer Berlin Heidelberg, 1997, vol. 134, ch. 3, pp. 165-234.
85. M. Nofar, W. Zhu and C. B. Park, *Polymer*, 2012, **53**, 3341-3353.
86. S. H. Mahmood, M. Keshtkar and C. B. Park, *J. Chem. Thermodyn.*, 2014, **70**, 13-23.
87. J. Reignier, J. Tatibouët and R. Gendron, *J. Appl. Polym. Sci.*, 2009, **112**, 1345-1355.
88. R. Kose and T. Kondo, *J. Appl. Polym. Sci.*, 2013, **128**, 1200-1205.
89. N. Chapleau, M. A. Huneault and H. Li, *Int. Polym. Proc.*, 2007, **22**, 402-409.
90. T. Alfrey, *Int. J. Polymer. Mater.*, 1979, **7**, 83-92.
91. P. Krishnamachari, J. Zhang, J. Lou, J. Yan and L. Uitenham, *Int. J. Polym. Anal. Charact.*, 2009, **14**, 336-350.
92. A. N. Frone, S. Berlioz, J. F. Chailan and D. M. Panaitescu, *Carbohydr. Polym.*, 2013, **91**, 377-384.
93. P. Pan, Z. Liang, B. Zhu, T. Dong and Y. Inoue, *Macromolecules*, 2009, **42**, 3374-3380.
94. X. Chen, J. Kalish and S. L. Hsu, *J. Polym. Sci., Part B: Polym. Phys.*, 2011, **49**, 1446-1454.
95. P. Pan, B. Zhu, W. Kai, T. Dong and Y. Inoue, *Macromolecules*, 2008, **41**, 4296-4304.
96. H. Marubayashi, S. Asai and M. Sumita, *Polymer*, 2012, **53**, 4262-4271.
97. H. Marubayashi, S. Akaishi, S. Akasaka, S. Asai and M. Sumita, *Macromolecules*, 2008, **41**, 9192-9203.
98. C. B. Park, L. K. Cheung and S. W. Song, *Cell. Polym.*, 1998, **17**, 221-251.
99. X. Xu, C. B. Park, D. Xu and R. Pop-Iliev, *Polym. Eng. Sci.*, 2003, **43**, 1378-1390.
100. J. W. Gibbs, *The Scientific Papers of J. Willard Gibbs*, Dover Publications, Inc. New York, 1961.
101. S. N. Leung, C. B. Park and H. Li, *Plast., Rubber Compos.*, 2006, **35**, 93-100.
102. S. N. Leung, C. B. Park and H. Li, *J. Cell. Plast.*, 2010, **46**, 441-460.
103. A. Wong, R. K. M. Chu, S. N. Leung, C. B. Park and J. H. Zong, *Chem. Eng. Sci.*, 2011, **66**, 55-63.
104. W. Zhai, Y. Ko, W. Zhu, A. Wong and C. B. Park, *Int. J. Mol. Sci.*, 2009, **10**, 5381-5397.
105. J. Wang, W. Zhu, H. Zhang and C. B. Park, *Chem. Eng. Sci.*, 2012, **75**, 390-399.
106. C. B. Park, D. F. Baldwin and N. P. Suh, *Polym. Eng. Sci.*, 1995, **35**, 432-440.